Enhancement of Low-Voltage-Ride-Through Capability for DFIG Wind Energy Systems

Xianghua Shi, Hui Ding, Yi Qi, Yi Zhang, Shaahin Filizadeh

***Abstract*--With increasing wind energy integration, grid codes require low-voltage ride-through (LVRT) compliance to ensure stability and prevent economic losses. This paper focuses on achieving LVRT in doubly fed induction generator (DFIG) based systems using positive- and negative-sequence component control. The delayed signal cancellation (DSC) method is compared with common techniques based on the second-order generalized integrator (SOGI), T/4 delay and low-pass or notch filter methods, demonstrating its superior dynamic performance. A novel approach for rotor-current decomposition is proposed, transforming mixed-frequency signals into general unbalanced signals for DSC processing. Sequence-component control schemes based on DSC decomposition are developed following LVRT requirements. Controller hardware-in-loop (HIL) tests of a 2.5-MW wind turbine validate the strategy's effectiveness in mitigating grid faults and enhancing LVRT performance.**

***Keywords*: wind energy, sequence decomposition, sequence-component control, DFIG, LVRT, delayed signal cancellation.**

I. Introduction

THE rapid growth of renewable energy has positioned wind energy as a key solution for sustainable power generation. Among wind turbine technologies, doubly fed induction generators (DFIGs) are widely used due to their high energy capture efficiency, flexible control of active and reactive power, and reduced power converter costs [1]-[4]. As wind penetration increases, grid codes mandate low-voltage ride-through (LVRT) compliance, requiring turbines to stay connected during voltage dips to maintain grid stability. Non-compliance can result in power instability, revenue loss, and penalties, emphasizing the need for robust LVRT strategies.

Unlike turbines with permanent-magnetic synchronous machines or induction machines, which are not directly connected to the AC grid, DFIG-based systems are directly impacted by grid faults, affecting both the grid-side converter (GSC) and the machine-side converter (MSC) [1]-[4]. Effective LVRT in DFIG systems require precise control of GSC and MSC currents to mitigate voltage sags and maintain stability. Sequence-component control techniques play a vital role in addressing asymmetries caused by grid faults, relying on decomposition of voltages and currents in GSC and MSC.

During unsymmetrical grid faults, the stator voltages and currents in DFIG systems exhibit frequencies of f_s and $-f_s$, where f_s is the grid frequency, representing general unbalanced signals. Common decomposition methods include the second-order generalized integrator (SOGI)-based method [5], the T/4 delay method, the delayed signal cancellation (DSC) method [6], and the filter-based method [7]-[9]. The SOGI- and filter-based methods generally have low bandwidth, which introduces substantial delays, impacting system stability. In contrast, the T/4 delay method, with a fixed one-quarter fundamental period delay, offers relatively better performance. Among these methods, the DSC method is particularly notable due to its adjustable delay, offering greater flexibility, and is adopted in this study due to its superior dynamic performance.

Rotor-side currents in DFIG systems under unbalanced faults exhibit two distinct frequencies, $s{\cdot}f_s$ and $(s\text{-}2){\cdot}f_s$, representing mixed-frequency signals, where s represents the slip, making traditional decomposition methods like SOGI-based, T/4 delay, and DSC methods ineffective. Existing solutions use notch [7]-[8] or low-pass (LP) [9] filter to separate components. While there are various implementations of filter-based methods for extracting rotor-current sequence components [7]-[9], they share the common principle of filtering out the double-line-frequency component. But these methods have limitations. Notch filters struggle with significant ripple responses with slow decay during transient disturbances, while LP filters with narrow bandwidths severely restrict the response speed of rotor-current decomposition during disturbances. To address these issues, this paper proposes a novel method that transforms mixed-frequency signals into general unbalanced signals, enabling the use of DSC method. This approach leverages the DSC method's strengths to achieve faster and more effective rotor-current decomposition.

In the context of DFIG-based wind energy systems, existing LVRT methods primarily address excessive energy dissipation during faults, employing approaches such as modified vector control [12-13], model predictive control (MPC)-based strategies [14-16], and advanced energy-absorbing schemes [17-18]. While modified vector control and MPC offer robust performance, they often come with higher computational demands and implementation challenges. In contrast, the proposed control strategy retains the simplicity of dual-loop control structures, widely adopted in the industry, ensuring both feasibility and cost-effectiveness. Excessive energy dissipation during faults is managed using a DC chopper or crowbar. The proposed LVRT strategy primarily focuses on reactive power support while also addressing key control objectives such as torque ripple suppression and balanced stator currents. Additionally, it introduces a

This work was supported by RTDS Technologies Inc.

X. Shi*, H. Ding, Y. Qi, and Y. Zhang are with RTDS Technologies Inc., Winnipeg, Canada (e-mail of authors: shixianghua1988@gmail.com, hui.ding@ametek.com, yi.qi@ametek.com, and yi.zhang@ametek.com).
S. Filizadeh is with the Department of Electrical Engineering, University of Manitoba, Winnipeg, Canada (e-mail: shaahin.filizadeh@umanitoba.ca).

Paper submitted to the International Conference on Power Systems Transients (IPST2025) in Guadalajara, Mexico, June 8-12, 2025.

distributed approach to reactive power sharing between the stator and GSC. Another key aspect, often overlooked in existing literature, is the suppression of negative-sequence voltage, which is also a focus of this study.

This paper focuses on LVRT capability in DFIG-based wind systems using a back-to-back (BTB) two-level voltage-source converter (2L-VSC) (see Fig. 1). Section II presents the DFIG model to guide the controller design. Section III compares the sequence-component extraction methods and proposes a novel rotor-current extraction method. Section IV introduces sequence-component control schemes for LVRT. Section V validates the proposed strategy through hardware-in-loop (HIL) test, and Section VI concludes the study.

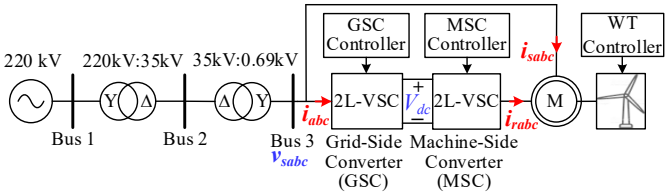

Fig. 1. DFIG wind energy system with BTB 2L-VSC.

II. Mathematical Modelling of DIFG

The dynamic modelling of DFIG wind energy systems has been extensively discussed in literatures [1]-[10]. This section provides a concise summary of the modelling, focusing on facilitating the design of sequence-component control schemes for the MSC. The voltage and flux equations are expressed as:

$$\begin{aligned} \overrightarrow{v_s} &= R_s \cdot \overrightarrow{\imath_s} + d\overrightarrow{\lambda_s}/dt \\ \overrightarrow{v_r'} &= R_r' \cdot \overrightarrow{\imath_r'} + d\overrightarrow{\lambda_r'}/dt - j\omega_r \overrightarrow{\lambda_r'} \end{aligned} \tag{1}$$

$$\begin{aligned} \overrightarrow{\lambda_s} &= L_s \cdot \overrightarrow{\imath_s} + L_m \cdot \overrightarrow{\imath_r'} \\ \overrightarrow{\lambda_r'} &= L_m \cdot \overrightarrow{\imath_s} + L_r' \cdot \overrightarrow{\imath_r'} \end{aligned} \tag{2}$$

In the above equations, L_m represents the mutual inductance, and ω_r denotes the rotor electrical angular speed. Parameters R_s (R_r'), L_s (L_r'), $\overrightarrow{\lambda_s}$ ($\overrightarrow{\lambda_r'}$), $\overrightarrow{v_s}$ ($\overrightarrow{v_r'}$) and $\overrightarrow{\imath_s}$ ($\overrightarrow{\imath_r'}$) correspond to the stator-side (rotor-side) resistance, self-inductance, flux, voltage and current vectors, respectively. The superscript "′" indicates rotor-side quantities are reflected to the stator side.

To account for both the negative- and positive-sequence components, a vector can be expressed as follows:

$$\vec{X} = \overrightarrow{X_{dq}^{p}} e^{j\omega_s t} + \overrightarrow{X_{dq}^{n}} e^{-j\omega_s t} \tag{3}$$

In this expression, $\vec{X}$ represents a space vector of voltage, current or flux. The superscripts "p" and "n" denote the positive- and negative-sequence components, respectively, while the subscript "dq" refers to the quantities in dq domain. The ω_s and $-\omega_s$ indicate the synchronous rotating speeds of the positive- and negative-sequence components, respectively.

Rewriting (1) and (2) using the vector form in (3), and transforming them into the positive- and negative-sequence synchronous rotating reference frames, the stator- and rotor-side equations in dq domain can be expressed as:

$$\begin{aligned} \overrightarrow{v_{sdq}^{x}} &= R_s \cdot \overrightarrow{\imath_{sdq}^{x}} + d\overrightarrow{\lambda_{sdq}^{x}}/dt + j(y \cdot \omega_s)\overrightarrow{\lambda_{sdq}^{x}} \\ \overrightarrow{v_{rdq}^{x}}' &= R_r' \cdot \overrightarrow{\imath_{rdq}^{x}}' + d\overrightarrow{\lambda_{rdq}^{x}}'/dt + j(y \cdot \omega_s - \omega_r)\overrightarrow{\lambda_{rdq}^{x}}' \end{aligned} \tag{4}$$

where x denotes letter "p" for positive-sequence and y = 1, while x represents letter "n" for negative-sequence and y = -1.

Subsisting $\overrightarrow{\lambda_r'}$ expressed in (2) and transformed to dq domain, the rotor-side dynamic modelling in (4) is derived as follows:

$$\begin{aligned} \overrightarrow{v_{rdq}^{x}}' = \; & R_r' \cdot \overrightarrow{\imath_{rdq}^{x}}' + L_{req}' d\overrightarrow{\imath_{rdq}^{x}}'/dt \\ & + j \cdot s^x \cdot \omega_s L_{req}' \overrightarrow{\imath_{rdq}^{x}}' + j \cdot s^x \cdot \omega_s \frac{L_m}{L_s} \overrightarrow{\lambda_{sdq}^{x}} \end{aligned} \tag{5}$$

where $L_{req}' = (L_r' L_s - L_m^2)/L_s$, x denotes letters "p" and "n", $s^p = s$, and $s^n = (s - 2)$ with the slip $s = (\omega_s - \omega_r)/\omega_s$.

The torque calculation is expressed as below.

$$T_e = \frac{3}{2}\frac{L_m}{L_s} n_p Im\left[\overrightarrow{\lambda_s} \cdot \widehat{\overrightarrow{\imath_r'}}\right] = T_{e0} + T_{esin2} + T_{ecos2} \tag{6}$$

where n_p is the number of pole pairs, and

$$\begin{bmatrix} T_{e0} \\ T_{esin2} \\ T_{ecos2} \end{bmatrix} = \frac{3}{2}\frac{L_m}{L_s} n_p \cdot A \cdot \begin{bmatrix} {i_{rd}'}^{p} \\ {i_{rq}'}^{p} \\ {i_{rd}'}^{n} \\ {i_{rq}'}^{n} \end{bmatrix} \tag{7}$$

with

$$A = \begin{bmatrix} \lambda_{sq}^{p} & -\lambda_{sd}^{p} & \lambda_{sq}^{n} & -\lambda_{sd}^{n} \\ -\lambda_{sd}^{n} & -\lambda_{sq}^{n} & \lambda_{sd}^{p} & \lambda_{sq}^{p} \\ \lambda_{sq}^{n} & -\lambda_{sd}^{n} & \lambda_{sq}^{p} & -\lambda_{sd}^{p} \end{bmatrix}$$

In DFIG applications, three-phase signals are typically transformed into dq domain using an angle aligned with either the stator voltage [10] or the stator flux [11]. Defining $\theta_{\lambda sq}{}^{p}$ as the positive-sequence stator-flux angle and using it for positive-sequence component transformation, it follows that $\lambda_{sq}{}^{p} = 0$. For the negative-sequence, using $-\theta_{\lambda sq}{}^{p}$ as the transformation angle avoids the need to track the negative-sequence stator-flux. This is beneficial since the negative-sequence stator flux may be very small and challenging to track accurately, which depends heavily on faulty conditions.

III. Sequence-Component Decomposition

In DFIG applications, asymmetrical faults generate negative-sequence stator voltages, inducing rotor currents at two distinct frequencies. This section discussed existing methods for sequence-component extraction and proposes an enhanced approach to decompose mixed-frequency signals.

A. Sequence-Component Decomposition for General Unbalanced Signals

Efficient sequence-component extraction methods are crucial for controlling sequence components and fall into two categories: those for general unbalanced signals (e.g., SOGI, T/4 delay, and DSC in Fig. 2) and those for both general and mixed-frequency unbalanced signals (e.g., LP filter, and notch filter in Fig. 3). Signal frequencies under asymmetrical grid conditions are annotated with "{}" in Fig. 2 and Fig. 3 and also apply to Fig. 5, where s represents the slip.

The SOGI method uses a second-order filter to obtain orthogonal signals, with the control parameter (k_{SOGI}) balancing response speed and harmonic suppression. Its feedback loop introduces a one-timestep delay, which reduces accuracy in amplitude and phase angle calculations, particularly in dynamic or rapidly changing grid conditions. To compensate the delay-induced inaccuracy, correction techniques are needed for SOGI [19]. On the other hand, the

DSC method uses trigonometric transformations and stores delayed data, and particularly, it offers greater flexibility as it allows for the adjustment of delay, enabling fine-tuned responses to dynamic system conditions. The T/4 delay method is simpler, straightforwardly utilizing a fixed T/4 delayed data to obtain orthogonal signals but lacks flexibility to reduce delay.

All decomposition methods for general unbalanced signals in Fig. 2 and Fig. 3 (with the slip s =1) are compared. Fig. 4 shows the dynamic responses of the root-mean-squared (RMS) values of positive- and negative-sequence voltages. At t =0.01s, symmetrical voltages (1.0pu, 50Hz) are altered to asymmetrical voltages with 0.8pu V_m^p and 0.1pu V_m^n. The LP filter employs a 25Hz bandwidth (-3dB) to filter out 100Hz ripple, while the notch filter is tuned to 100Hz with a 5Hz bandwidth (quality factor of 20). The comparisons of all methods are presented in two separate graphs to avoid excessive plot overlap in a single graph: the left graph for SOGI and filter-based methods, and the right graph for DSC and T/4 delay methods. It is observed that the SOGI method takes ~0.05s to reach steady state for k_{SOGI} = 0.4. Increasing k_{SOGI} improves the response speed but introduces large ripples and slow decay, requiring a tradeoff in parameter selection. The LP filter method settles in ~0.02s with relatively minimal ripple, while the notch filter method exhibits significant oscillation. In contrast, the DSC method reaches steady state within its configured delay time (generally ≤T/4, i.e., ≤5ms for a 50Hz system). When set to T/4, the DSC method performs identically to the T/4 delay method. However, DSC allows for a smaller delay less than T/4, enabling a faster response.

Overall, the DSC method offers superior performance and flexibility compared to SOGI, T/4 delay, and filter-based methods, particularly in response speed and ripple suppression. However, it cannot be directly applied to extract rotor currents with mixed frequencies, as discussed in the next subsection.

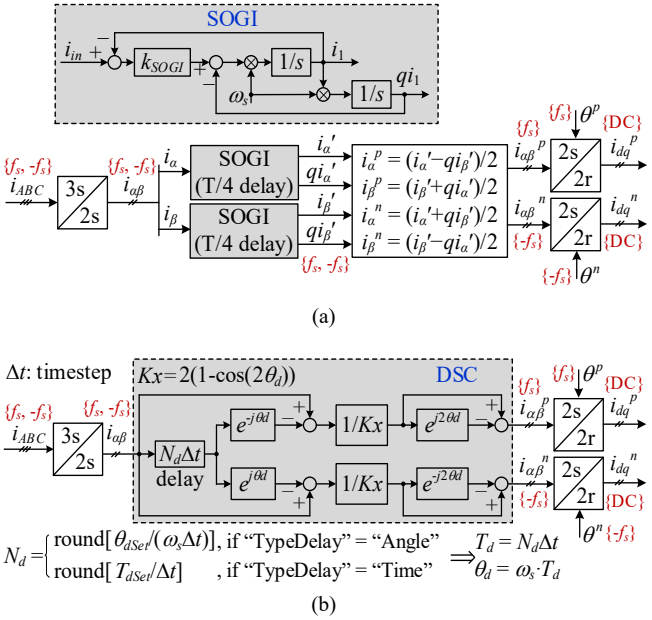

(a)

(b)

Fig. 2. Sequence-component decomposition methods only for general unbalanced signals based on (a) SOGI or T/4 delay, and (b) DSC.

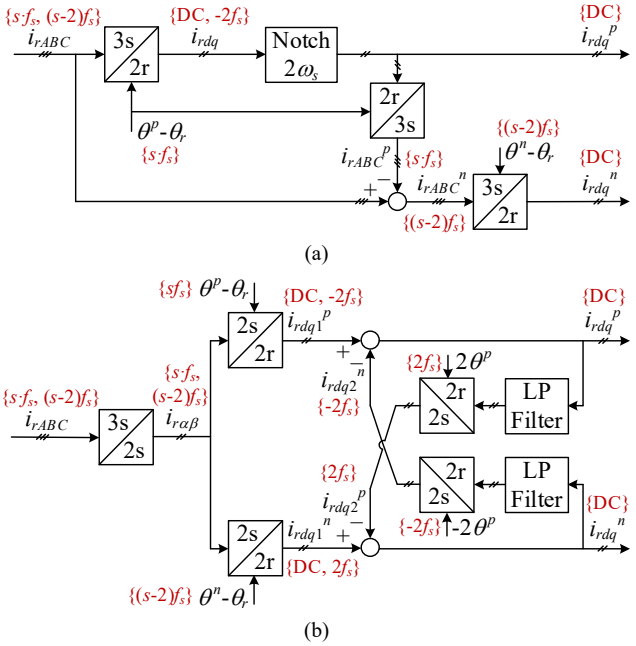

(a)

(b)

Fig. 3. Sequence-component decomposition methods for general unbalanced and mixed-frequency signals based on (a) notch filter, and (b) LP filter.

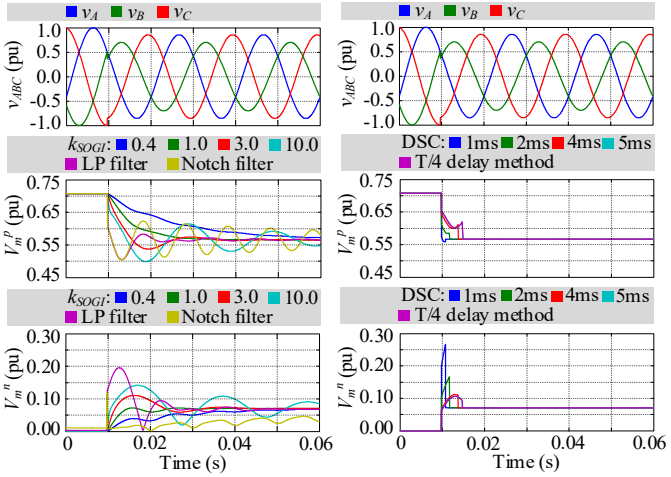

Fig. 4. Dynamic response of RMS values of positive- and negative-sequence voltages using decomposition methods based on SOGI, LP filter, notch filter, DSC and T/4 delay.

B. Sequence-Component Decomposition for Mixed-frequency Signals

Rotor currents in DFIG exhibit mixed frequencies under unbalanced faults, requiring effective frequency separation techniques. Conventional methods, illustrated in Fig. 3, employ rotating frames with speeds of $s{\cdot}2\pi f_s$ and $(s\text{-}2){\cdot}2\pi f_s$ to transform rotor current signals. However, this approach leads to the overlapping of $2f_s$ components, typically mitigated using notch or LP filters, which introduce slow response and potential oscillation issues. To overcome these limitations, a modified DSC method for decomposing mixed-frequency signals is proposed, as shown in Fig. 5. The preprocessing step transforms the three-phase input signal into a rotating reference frame using a 3s/2r transformation, aiming to convert the mixed-frequency signals into general unbalanced signals. Denoting the original frequencies in the three-phase signals as f_1 and f_2, the transformed two-phase signal, i_{r2ph}^{ST},

exhibits new frequencies given by:

$$f_{new1} = f_1 - f_{angle}$$
$$f_{new2} = f_2 - f_{angle} \quad (8)$$

where f_{angle} represents the transformation angle's frequency. To ensure that $i_{r2ph}{}^{ST}$ becomes general unbalanced signals, it must satisfy $f_{new1} = -f_{new2}$, requiring the transformation angle's frequency to be $(f_1+f_2)/2$. In DFIG's operation, there is

$$f_{angle} = \frac{s \cdot f_s + (s-2) \cdot f_s}{2} = (s-1) \cdot f_s \quad (9)$$

Notably, this frequency matches the negative frequency of the DFIG rotor's rotational speed. Consequently, the negative rotor angle ($-\theta_r$) is selected as the transformation angle, as depicted in Fig. 5. To decompose the general unbalanced signal $i_{r2ph}{}^{ST}$, all methods shown in Fig. 2 (i.e., SOGI, T/4 delay and DSC) can be applied. However, the DSC method is preferred due to its superior performance over the alternatives, as discussed in Section III.A.

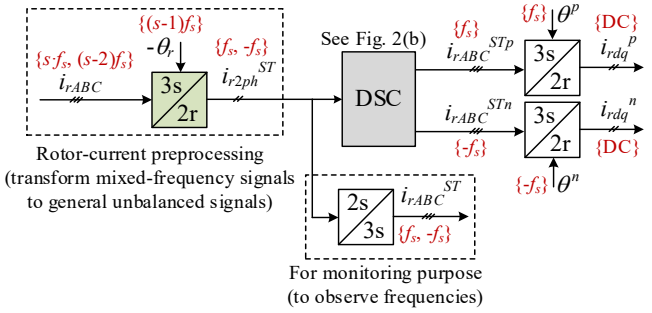

Fig. 5. Proposed rotor-current extraction using the modified DSC method.

Taking the DFIG operation at a 50Hz frequency with a slip of s = -0.35 (i.e., generator mode) as example, the rotor currents operate at -17.5Hz and -117.5Hz during unbalanced grid faults. At t =0.1s, the symmetrical rotor currents (1.0pu at -17.5Hz) change to 0.8pu at -17.5Hz and 0.2pu at -117.5Hz. Fig. 6 shows the dynamic response of decomposition using the notch filter, LP filter, and the modified DSC methods.

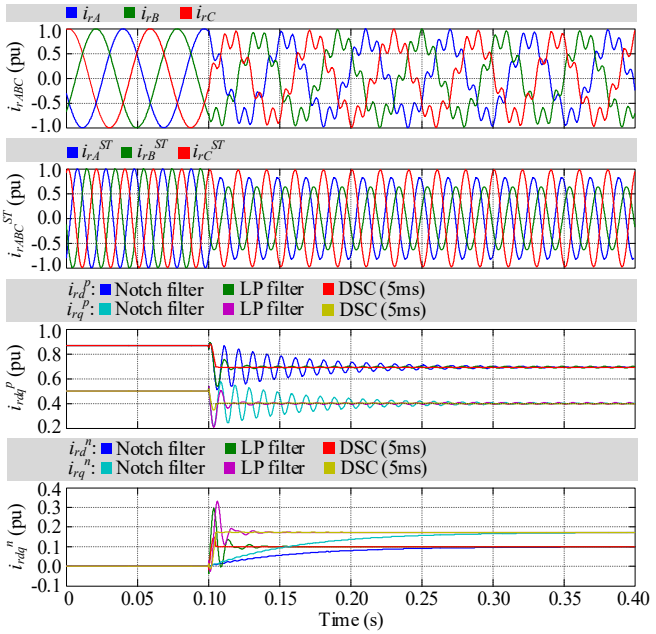

Fig. 6. Dynamic response of rotor-current decomposition based on the notch filter, LP filter and modified DSC methods.

It is observed that the proposed method initially transforms rotor currents to ±50Hz components (see $i_{rABC}{}^{ST}$ plot in Fig. 6). The rotor-current dq components ($i_{rdq}{}^{p}$ and $i_{rdq}{}^{n}$) using notch filter method exhibits significant oscillations and slow decay (taking ~0.2s to reach steady state), while these signals under the LP filter method performs better but still takes ~0.05s to reach steady state. In contrast, the modified DSC method with 5ms delay setting achieves steady state within 5ms, matching its configured delay time (or even shorter with smaller delay setting). Therefore, with the rotor-current preprocessing step, the mixed-frequency signal separation successfully leverages the advantages of DSC method.

IV. Sequence-Component Control of DFIG with LVRT Considerations

This section presents the sequence-component control strategies for the GSC and MSC and emphasizes the key considerations for LVRT. Compared to advanced technologies [12]-[19], the proposed strategy maintains the simplicity of dual-loop control structures, which are widely adopted in the industry, ensuring both feasibility and cost-effectiveness. Moreover, with advancements in modern processors and computational hardware, the implementation complexity is no longer a significant concern for digital controllers.

A. Sequence-Component Control for GSC

Fig. 7 shows the GSC sequence-component control using the DSC method to extract sequence components. The positive-sequence dq-axis align with the stator-voltage phase (θ^p), while the negative-sequence frame is set to $\theta^n = -\theta^p$. Outer loops regulate the DC-link voltage and AC voltage magnitude, producing positive-sequence dq-axis current references ($i_d{}^{p*}$ and $i_{q\_tot}{}^{p*}$). Reactive power is shared between the GSC and MSC, with the GSC's contribution defined by k_{GSC} ($0 \le k_{GSC} \le 1$), while the MSC adjusts the remaining reactive power via the stator current reference ($i_{sd}{}^{p*}$). Negative-sequence currents can suppress unbalanced voltage but are usually set to zero for balanced AC currents during faults. A decoupled control strategy governs both positive- and negative-sequence components, combing them into voltage references for modulation waveform generation.

Proper proportional-integral (PI) controller limits are critical to fulfill control functions. During faults, the reactive power support is prioritized, making q-axis current control more critical than d-axis. The q-axis current limit is determined by the maximum reactive power (Q_{max}):

$$I_{qMax}^{p} = |Q_{max}/(-1.5 \cdot v_{sd}^{p})| \quad (10)$$

where $v_{sd}{}^{p} = V_{sm}{}^{p}$ as the transformation angle is aligned with the stator voltage. The d-axis current limit is based on the maximum current (I_{max}) and the q-axis current reference ($i_q{}^{p*}$):

$$I_{dMax}^{p} = \sqrt{I_{max}^{2} - i_{q}^{p*2}} \quad (11)$$

B. Sequence-Component Control for MSC

Fig. 8 shows the MSC's sequence-component control diagram based on (5). The DSC method is used for voltage and current decomposition from the stator sides, while rotor current extraction employs the modified DSC from Fig. 5. The

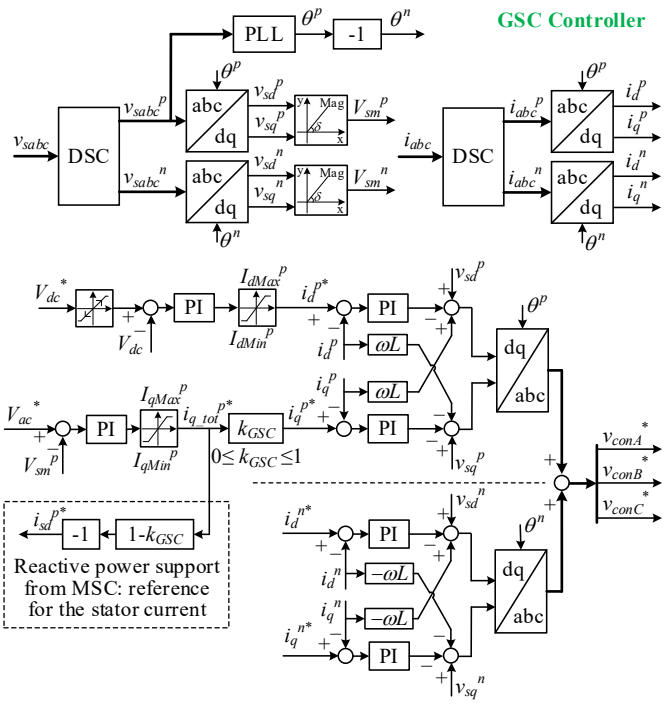

Fig. 7. Sequence-component control for the GSC in DFIG applications.

dq transformation angle aligns with the positive-sequence stator flux (i.e., $\theta_{\lambda s}^{p}$), with the negative-sequence set as $\theta_{\lambda s}^{n} = -\theta_{\lambda s}^{p}$. The outer loop controls torque for maximum power point tracking (MPPT) or limited power operation, generating the positive-sequence q-axis rotor current reference (i_{rq}^{p*}). The positive-sequence d-axis rotor current reference (i_{rd}^{p*}) provides reactive power support and is calculated using (2) as:

$$i_{rd}^{p\,*} = \frac{\lambda_{sd}^{p}}{L_m} - \frac{L_s}{L_m} i_{sd}^{p\,*} \tag{12}$$

where $\lambda_{sd}^{p} = \lambda_{sm}^{p}$, and $i_{sd}^{p*} = -(1-k_{GSC})\cdot i_{q\_tot}^{p*}$ (see Fig. 7). Due to reference frame difference, the q-axis current at the GSC corresponds to the negative d-axis current at the MSC.

Negative-sequence current can eliminate torque/reactive power oscillations, suppress active power oscillations, or balance stator and rotor currents [10]-[11]. For balanced current control, simply set $i_{rd}^{n*} = i_{rq}^{n*} = 0$. To eliminate torque oscillations, setting $T_{esin2} = T_{ecos2} = 0$ (see (7)) results in:

$$\begin{aligned} i_{rd}^{n\,*} &= \frac{\lambda_{sq}^{n} \cdot i_{rq}^{p\,*} + \lambda_{sd}^{n} \cdot i_{rd}^{p\,*}}{\lambda_{sd}^{p}} \\ i_{rq}^{n\,*} &= \frac{\lambda_{sq}^{n} \cdot i_{rd}^{p\,*} - \lambda_{sd}^{n} \cdot i_{rq}^{p\,*}}{\lambda_{sd}^{p}} \end{aligned} \tag{13}$$

Like the GSC, the MSC provides reactive power support during faults. The positive-sequence q-axis rotor current limit is determined by the maximum rotor current (I_{rmax}) and the positive-sequence d-axis current reference (i_{rd}^{p*}):

$$I_{rqMax}^{p} = \sqrt{I_{rmax}^{2} - i_{rd}^{p*2}} \tag{14}$$

Unbalanced faults induce a $(s\text{-}2)\cdot f_s$ frequency component in the rotor current, leading to significant voltage drops across inductance (L_{req}'), potentially causing overmodulation. Based on superposition theorem and large frequency difference ($s\cdot f_s$ and $(s\text{-}2)\cdot f_s$ with s typically within [-0.35, 0.35]), the rotor-side modulation waveform peaks at $\sim(m_r^{p} + m_r^{n})$, or $\sim(m_r^{p}/1.15+ m_r^{n})$ with 3rd harmonic injection to the positive-sequence modulation waveform, where m_r^{p} and m_r^{n} are the positive- and negative-sequence modulation indices, respectively. To prevent overmodulation, the negative-sequence modulation index is limited to $(1 - m_r^{p})$ or $(1.15 - m_r^{p}/1.15)$ with 3rd harmonic injection.

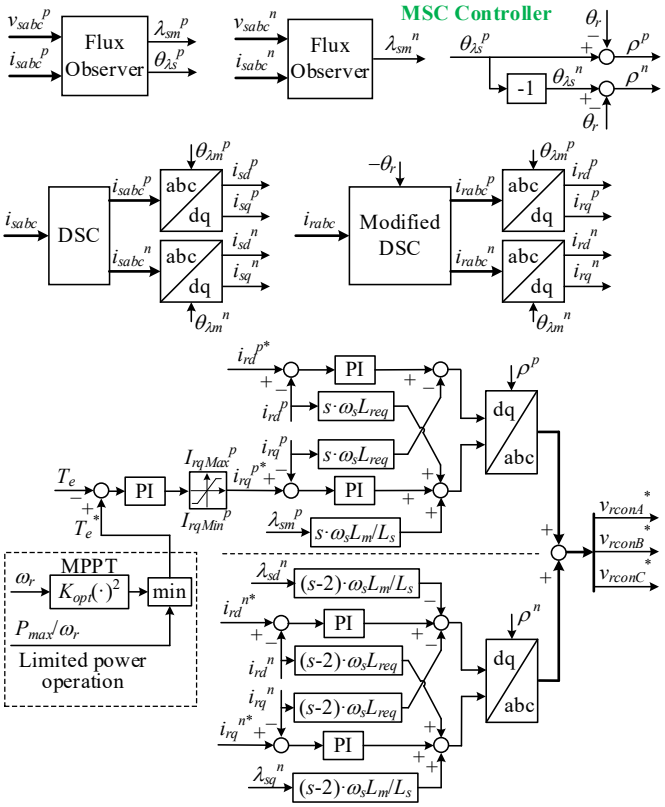

Fig. 8. Sequence-component control for MSC in DFIG applications.

C. LVRT Considerations

Fault ride-through requirements differ by country and application. This paper adopts the standards from GB/T 19963 [20], which regulate wind farm connections to power systems in China. Fig. 9 illustrates the fault detection mechanism for high- and low-voltage conditions. It evaluates positive- and negative-sequence voltage magnitudes and generates three flags based on the specified criteria:

- *LVFlag*: 1 for a low-voltage fault, otherwise 0.
- *HVFlag*: 1 for a high-voltage fault, otherwise 0.
- *SysFltFlag*: 1 for an unbalanced fault, otherwise 0.

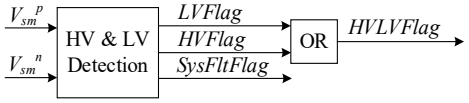

Fig. 9. Simplified diagram for AC grid fault detection.

(i) Reactive-Power Support

Fig. 10 illustrates the AC voltage control loop, designed according to GB/T 19963 fault-ride-through codes. During faults, the GSC provides reactive power support by adjusting the positive-sequence q-axis current reference, $i_{q\_tot}^{p(new)*}$, combining the pre-fault value ($i_{q\_tot}^{p*}$) with an increment (ΔI_q^{p}). A sample-and-hold component preserves $i_{q\_tot}^{p*}$ during fault detection delays, while the fault detection flag determines ΔI_q^{p}.

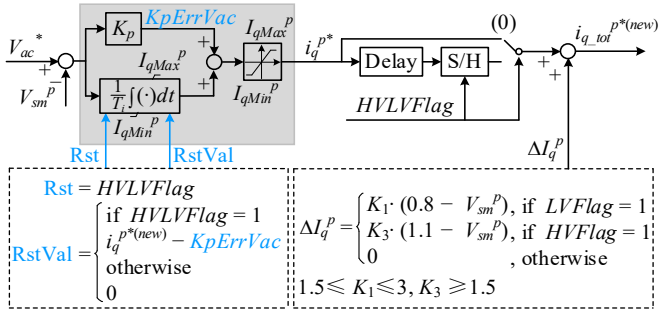

Fig. 10. AC voltage control-loop modifications with LVRT considerations.

Rapid q-axis reference changes can cause voltage spikes and misdetect fault types. To ensure stability and accurate detection, the q-axis current reference must transition smoothly during fault clearance. This is achieved by resetting the PI controller integrator during faults (i.e., $HVLFVlag$ = 1) with a value of ($i_q^{p*(new)}$ – $KpErrVac$).

(ii) Suppression of Negative-Sequence Voltage

To mitigate unbalanced voltage during grid faults, appropriate negative-sequence current must be injected or absorbed by the AC system. The negative-sequence operation is described as:

$$\overrightarrow{V_{pcc}^n} = \overrightarrow{V_s^n} + \overrightarrow{I^n} \cdot j(-\omega_s)L_{eq} \tag{15}$$

where $\overrightarrow{V_s^n}$ is the negative-sequence voltage vector at the controlled AC bus, $\overrightarrow{V_{pcc}^n}$ is at the PCC, $\overrightarrow{I^n}$ is current vector flowing from the grid to the controlled AC bus, and L_{eq} is the equivalent inductance between the grid and controlled AC bus. By controlling $\overrightarrow{I^n}$ to lead $\overrightarrow{V_s^n}$ by 90°, the voltage across the equivalent inductor ($-j\omega_s L_{eq}\overrightarrow{I^n}$) aligns with $\overrightarrow{V_s^n}$, effectively minimizing $\overrightarrow{V_s^n}$ and mitigating voltage imbalance at the controlled bus. Fig. 11 illustrates the implementation of the negative-sequence current references for this purpose.

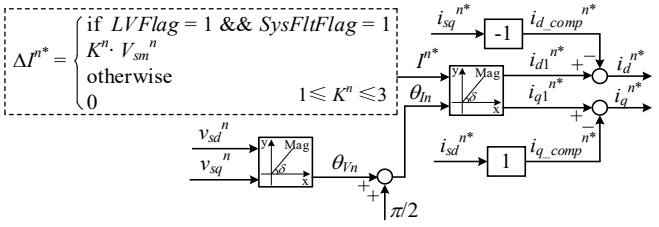

Fig. 11. Negative-sequence current references for reducing unbalanced voltages and compensating for negative-sequence stator currents.

As analyzed in Section IV.B, the MSC injects negative-sequence current for torque ripple suppression, leading to stator current unbalanced and worsening voltage imbalance. To minimize negative-sequence voltage, the GSC offsets negative-sequence stator currents by supplying negative-sequence current compensation. Based on (2), the induced negative-sequence stator currents (i_{sd}^{n*} and i_{sq}^{n*}) from rotor currents (i_{rd}^{n*} and i_{rq}^{n*}) are given below.

$$i_{sd}^{n\,*} = \frac{\lambda_{sd}^n}{L_s} - \frac{L_m}{L_s} i_{rd}^{n\,*}$$
$$i_{sq}^{n\,*} = \frac{\lambda_{sq}^n}{L_s} - \frac{L_m}{L_s} i_{rq}^{n\,*} \tag{16}$$

Due to 90-degree phase differences in reference frames between the GSC and MSC, the negative-sequence dq-axis stator currents reflect to the GSC reference frame as follows:

$$i_{d\_comp}^{n\,*} = -i_{sq}^{n\,*}$$
$$i_{q\_comp}^{n\,*} = i_{sd}^{n\,*} \tag{17}$$

To counter back the unbalanced stator currents from the MSC, $i_{d\_comp}^{n*}$ and $i_{q\_comp}^{n*}$ are subtracted from the i_{d1}^{n*} and i_{q1}^{n*}, respectively, as shown in Fig. 11.

V. Real-Time Simulation and Validation

The RTDS® platform simulates power system transients in real time using parallel processing and small time steps (≤50 µs), enabling real-time interaction with external controllers for HIL testing. In this study, the controller HIL methodology is applied to evaluate the control schemes of a DFIG-based wind energy system (Fig. 1) under fault conditions. The test setup (Fig. 12) models the power system on a 2.5-GHz NovaCor processor, while the controller runs on a PB5 card with two 1.7-GHz Freescale MC7448 RISC processors [21]. The computational timestep for HIL test is 50.0µs. The wind turbine is modeled as a single 2.5MW turbine, with a scaling transformer increasing the output 100-fold for grid connection. System parameters for the DFIG wind turbine, and AC grid and transformers are detailed in Tables I and II, respectively.

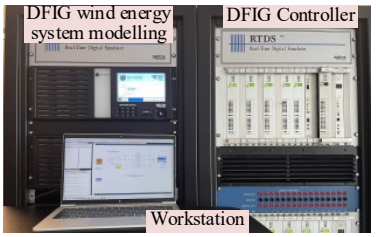

Fig. 12. Controller HIL test setup for DFIG wind energy system.

TABLE I
Parameters of Single DFIG Wind Turbine System

Rated power	2.5 MW	R_s	0.01 pu
Rated stator voltage	0.69 kV	R_r'	0.006 pu
Rated frequency	50 Hz	L_m	4.348 pu
Turns ratio (rotor/stator)	2.6377	L_{ls}	0.102 pu
Inertia constant	1.5 s	L_{lr}'	0.086 pu
DC-link capacitance	0.02 F	ω_r (at rated MPP)	1.35 pu
DC-link rated voltage	1.5 kV	s (at rated MPP)	-0.35
Rated power of GSC	0.26 pu	Rated power of MSC	0.74 pu

TABLE II
Parameters of the AC System and Transformers in Fig. 1

Transformer 1 (Scaling transformer)	220 kV: 35 kV, 50Hz, 2.5 MVA with 100 scale factor, 0.1 pu leakage, and 0.001 pu resistance
Transformer 2	35 kV: 0.69 kV, 50 Hz, 2.5 MVA, 0.1 pu leakage, and 0.001 pu resistance
AC grid	220 kV, 50 Hz, SCR = 3.56∠80°

The DFIG operates at a rated slip of -0.35, resulting in rated capacities of 0.26pu and 0.74pu for the GSC and MSC, respectively. The maximum reactive power support is set to Q_{max} =0.4pu, while the maximum current limits are configured as I_{max} =0.4pu (1.5 times the rated current) for GSC and I_{rmax} = 1.1pu (1.5 times the rated current) for MSC.

A. DFIG Operation Comparison under Different Rotor-Current Decompostion Methods

This paper focuses on sequence-component decomposition methods for DFIG's rotor current in LVRT control. Sections

III.A and III.B offer a preliminary analysis. This subsection aims to validate the modified DSC method in a DFIG-based wind energy system. By switching between the modified DSC and LP filter, notch filter, and SOGI (after rotor-current preprocessing to general unbalanced signals) methods, the system's waveforms are shown in Fig. 13, where two graphs with proper y-axis scales to show details. Results indicate that while the LP filter method introduces low-frequency ripples in power and torque, the system remains stable. The notch filter and SOGI methods cause stability issues and fault misdetection due to large delays. In contrast, the modified DSC method shows superior steady-state performance and effectively withstands disturbances. These highlight the advantages of the modified DSC method for practical DFIG-based wind energy systems.

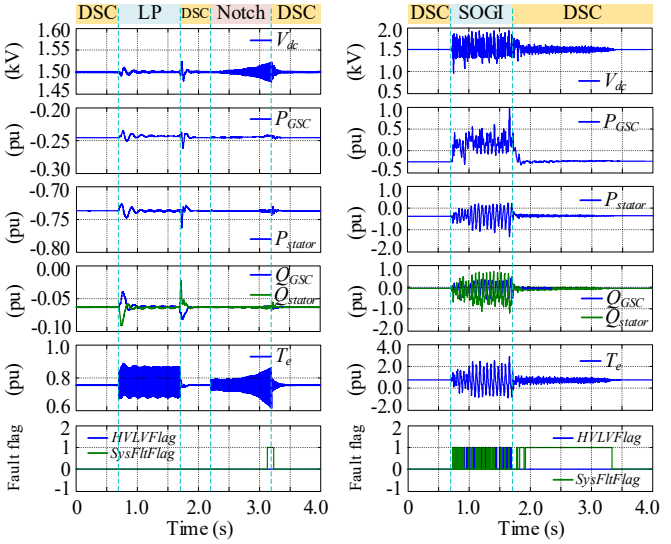

Fig. 13. Comparison of DFIG wind energy system operation under different rotor-current decomposition methods at 1.0pu power.

B. Symmetrical Fault Test

A symmetrical fault was introduced at t =0.4s, reducing the AC grid voltage from 1.0pu to 0.6pu for 1.0 second under two operating conditions (1.0pu and 0.5pu power). The simulation results, presented in Fig. 14 (left for 1.0pu power and right for 0.5pu power), demonstrate that the system successfully rides through the voltage dips, maintaining smooth transitions during fault initiation and clearance. The reactive power contributions from the GSC and the stator are approximately equal, with k_{GSC} =0.5, indicating shared support.

For 1.0pu power, the AC voltage drops to ~0.695pu, triggering fault detection and bypassing the AC voltage control loop. The pre-fault q-axis current remains ~0.14pu (as inferred from Q_{gsc}+Q_{stator} = -$v_{sd}{}^{p}{}_{(pu)}$·$i_{q\_tot}{}^{p}{}_{(pu)}$ ≈ -0.14 under normal operation), with additional reactive power support injecting ~0.21pu q-axis current based on K_1·(0.8 – $V_{smt}{}^{p}$) and K_1 =2.0, leading to a total q-axis current of ~0.35pu. Theoretical reactive power injection (-0.695×0.35 = -0.24pu) aligns with simulation results, where the GSC and MSC each contribute ~-0.12pu (see from Q_{gsc} and Q_{stator}). Following the similar analysis for 0.5pu power, the total reactive power contribution is ~-0.18pu, well matched with the simulation, where the GSC and MSC each contribute ~-0.09pu. These results confirm the effectiveness of the control strategies to provide reactive power support based on the LVRT rules, ensuring stable fault ride-through performance.

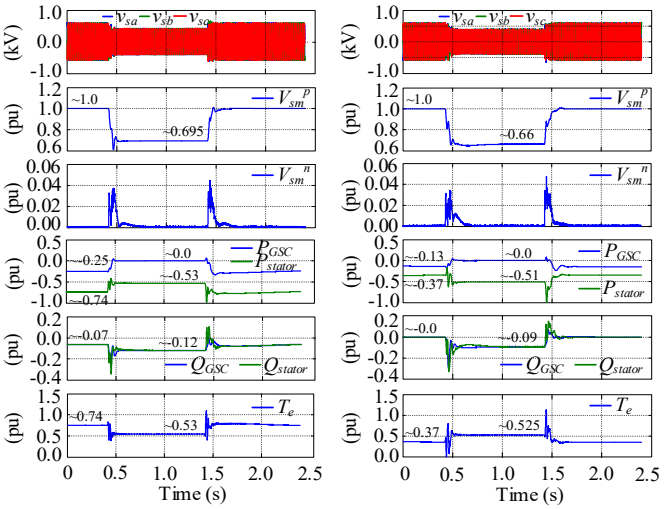

Fig. 14. Operation of the DFIG wind energy system under a symmetrical fault, with the AC grid voltage dropping from 1.0pu to 0.6pu, operating at 1.0pu power (left) and 0.5pu power (right).

C. Asymmetrical Fault Test

An asymmetrical fault was introduced by adjusting the AC grid voltage from 1.0pu in all phases to 0.7pu (phase A), 0.7pu (phase B), and 0.55pu (phase C) for both 1.0pu and 0.5pu power. The fault starts at t =0.4s and lasts 1.6 seconds. The simulation results, shown in Fig. 15 (left for 1.0pu power and right for 0.5pu power), evaluate two control objectives: balanced stator current control (Test I) and torque ripple suppression (Test II).

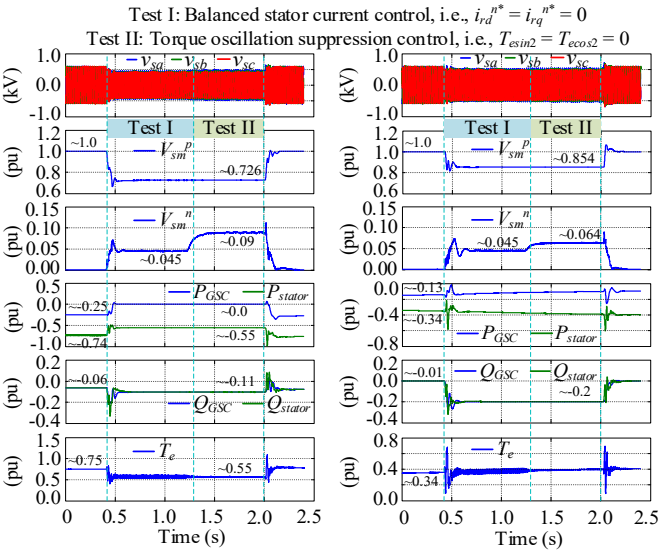

Fig. 15. Operation of the DFIG wind energy system under an asymmetrical fault, with the AC grid voltage dropping from 1.0pu (phases A, B, and C) to 0.7pu (phase A), 0.7pu (phase B) and 0.55pu (phase C), operating at 1.0pu power (left) and 0.5pu power (right).

The results show that it causes ripple in torque under balanced stator currents (see Test I) during asymmetrical faults, while the torque ripple is successfully suppressed (see Test II) by injecting negative-sequence current specified in (13). It is worth noting that during the transition from Test I to

Test II, the negative-sequence voltage at the controlled AC bus increases from ~0.045 pu to ~0.09 pu, indicating that suppressing torque oscillations increases grid imbalance.

D. Negative-Sequence Voltage Suppression Test

The fault condition from the previous subsection was further tested to evaluate negative-sequence suppression control with stator current compensation and varying negative-sequence current injection coefficients (K^n) as shown in Fig. 11. During the fault, the control progresses further through three stages: (i) torque oscillation suppression (Test I), (ii) compensation for negative-sequence stator current (Test II), and negative-sequence voltage suppression (Test III).

The simulation results are presented in Fig. 16 under 1.0pu power. It shows that negative-sequence voltage decreases from ~0.09pu to ~0.045pu when the GSC compensates for the negative-sequence stator current in Test II. Compared to Fig. 15, this compensation restores grid balance to the level achieved with balanced stator current control, demonstrating that torque ripple suppression no longer increases grid imbalance when compensation is applied. In Test III, further suppression of negative-sequence voltage from 0.045pu to 0.035pu is achieved, with greater suppression as K^n increases, improving overall grid balance.

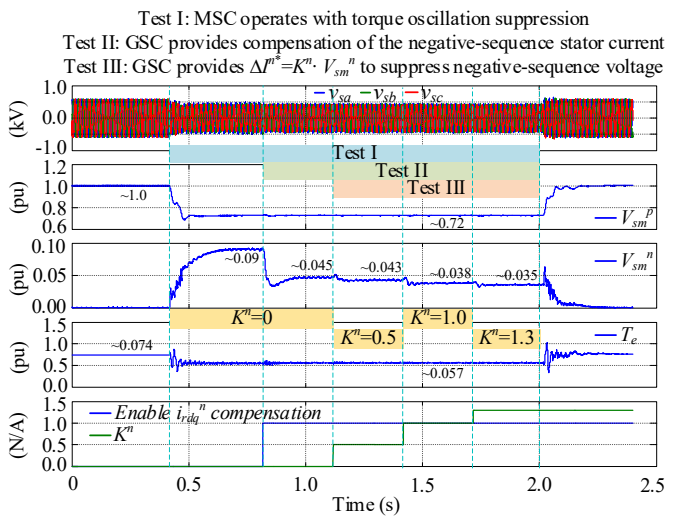

Fig. 16. DFIG wind energy system operation with negative-sequence voltage suppression under the asymmetrical fault with the AC grid voltage changing from 1.0pu (phases A, B, and C) to 0.7pu (phase A), 0.7pu (phase B) and 0.55pu (phase C) operating at 1.0pu power.

VI. Conclusions

This paper investigates methods to enhance LVRT capability in DFIG-based wind systems. It demonstrated that the DSC method offers superior dynamic response, accuracy, and flexibility compared to SOGI and filter-based methods. A modified DSC method was proposed to overcome the slow response limitations in rotor-current decomposition. The developed GSC and MSC control schemes effectively ensure fault ride-through by balancing stator currents, suppressing torque oscillations, and mitigating grid imbalances. HIL tests on a 2.5-MW wind turbine confirmed smooth fault transitions, robust grid support, and LVRT compliance, advancing the control strategies for modern grids.

VII. References

[1] S. Engelhardt, J. Kretschmann, J. Fortmann, F. Shewarega, I. Erlich and T. Neumann, "Capability and limitations of DFIG based wind turbines concerning negative sequence control," in *2013 IEEE PES Gen. Meet.*, pp. 1-5.

[2] P. Tourou, and C. Sourkounis, "Review of control strategies for DFIG-based wind turbines under unsymmetrical grid faults," in *2014 Int. Conf. Ecol. Veh. Renew. Energy (EVER)*, pp. 1-9.

[3] Y. Song, D. Zhou and F. Blaabjerg, "Improved DFIG Control Strategy Under Three-Phase Asymmetrical Grid Faults," in *2018 IEEE Energy Convers. Congr. Expo. (ECCE)*, pp. 5515-5520.

[4] M. Liu, Y. Xu and Z. Chen, "Coordinated control strategy of DFIG under grid voltage unbalance conditions," in *2010 Int. Conf. Crit. Infrastruct. (CRIS)*, pp. 1-5.

[5] P. Rodríguez, A. Luna, and R. Muñoz-Aguilar, "A stationary reference frame grid synchronization system for three-phase grid-connected power converters under adverse grid conditions," *IEEE Trans. Power Electron.*, vol. 27, pp. 99-112, Jan. 2012.

[6] R. Cárdenas, M. D´ıaz, F. Rojas, and J. Clare, "Fast convergence delayed signal cancellation method for sequence component separation," *IEEE Trans. Power Del.*, vol. 30, pp. 2055-2057, Aug. 2015.

[7] S. Yang, L. Zhan, C. Huang, and Z. Xie, "Unbalanced control system design for DFIG-based wind turbines," in *2012 Power Eng. Autom. Conf.*, pp. 1-4.

[8] M. M. Baggu, B. H. Chowdhury, and J. W. Kimball, "Comparison of advanced control techniques for grid side converter of doubly-fed induction generator back-to-back converters to improve power quality performance during unbalanced voltage dips," *IEEE J. Emerg. Sel. Topics Power Electron.*, vol. 3, pp. 516-524, Jun. 2015.

[9] J. Hu, "Investigation on the ride-through operation of DFIG-based wind power generation systems during grid fault," Ph.D. dissertation, Dept. Electr. Mach. Appl., Zhejiang Univ., 2009.

[10] Z. Zheng, G. Yang, and H. Geng, "Capability of asymmetrical grid faults ride-through for DFIG-based wind turbines," in *IECON 2012*, pp. 3533-3540.

[11] H. Jedtberg, M. Langwasser, R. Zhu, G. Buticchi and M. Liserre, "Impacts of rotor current control targets on DC-link capacitor lifetime in DFIG-based wind turbine during grid voltage unbalance," in *2017 IEEE Energy Convers. Congr. Expo. (ECCE)*, pp. 3489-3495.

[12] Y. Zhou, P. Bauer, J. Ferreira, and J. Pierik, "A modified vector control strategy for DFIG-based wind turbines to enhance LVRT capability," *IEEE Trans. Energy Convers.*, vol. 25, pp. 740-748, Sep. 2010.

[13] A. Boukhezzar and H. Siguerdidjane, "Modified vector-controlled DFIG wind energy system using robust predictive control," *Arab. J. Sci. Eng.*, vol. 48, pp: 1-25, Jul. 2024.

[14] J. Hu, Y. Huang, D. Wang, and H. Yuan, "Model predictive control for DFIG to improve the LVRT capability," *IEEE Trans. Ind. Electron.*, vol. 70, pp. 4289-4299, May 2023.

[15] M. Masoum, S. Deilami, and P. Moses, "Model predictive control for low-voltage ride through capability enhancement of DFIG under both balanced and unbalanced grid voltage dips," *IEEE Trans. Power Electron.*, vol. 32, pp. 624-637, Jan. 2017.

[16] K. Ouari, Y. Belkhier, H. Djouadi, A. Kasri, M. Bajaj, E. Elattar, and S. Kamel, "Improved nonlinear generalized model predictive control for robustness and power enhancement of a DFIG-based wind energy converter," *Front. Energy Res.*, vol. 10, pp. 1-13, Sep. 2022.

[17] M. Elshaer, M. Mosaad, and A. Abdelaziz, "Improved low voltage ride-through capability of DFIG-based wind turbines using series dynamic braking resistor," *IEEE Trans. Ind. Electron.,* vol. 65, pp. 2793-2801, Apr. 2018.

[18] A. Loulijat, H. Chojaa, M. Marghichi, N. Ettalabi, A. Hilali, A. Mouradi, A. Abdelaziz, Z. Elbarbary, and M. Mossa, "Enhancement of LVRT ability of DFIG wind turbine by an improved protection scheme with a modified advanced nonlinear control loop," *Processes*, vol. 11, pp. 1-25, May. 2023.

[19] X. Shi, S. Filizadeh, "Independent-phase current control of a three-phase VSC under unbalanced operating conditions," *J. Eng.*, vol. 2019, pp. 1338-1345, Feb. 2019.

[20] *Technical Specification for Connecting Wind Farm to Power System – Part 1: On Shore Wind Power*, GB/T 19963.1-2021, Aug. 2021.

[21] P. Mestas, M. Tavares and A. Gole, "Implementation and Performance Evaluation of a Reclosing Method for Shunt Reactor-Compensated Transmission Lines," in *IEEE Trans. Power Del.*, vol. 26, pp. 954-962, Apr. 2011.